Nonspherical and Spherical Characterization of Ice in Hurricane Erin for Wideband Passive Microwave Comparisons

Gail Skofronick-Jackson[1], Eric Holthaus[2], Cerese Albers[3], and Min-Jeong Kim[4]

1. NASA Goddard Space Flight Center, Greenbelt, MD
2. Columbia University, New York City, NY
3. Florida State University, Tallahassee, FL
4. NOAA, Camp Springs, MD

Submitted to Journal of Geophysical Research April 10, 2007

Corresponding Author: Gail Skofronick Jackson, Code 614.6, Building 33, Room A428, Greenbelt, MD 20771, 301-614-5720, FAX 301-614-5558, Gail.S.Jackson@nasa.gov

Popular Summary:

In order to better understand the characteristics of frozen cloud particles in hurricane systems, computed brightness temperatures were compared with radiometric observations of Hurricane Erin (2001) from the NASA ER-2 aircraft. The focus was on the frozen particle microphysics and the high frequencies (≥ 85 GHz) that are particularly sensitive to frozen particles. Frozen particles in hurricanes are an indicator of increasing hurricane intensity. In fact "hot towers" associated with increasing hurricane intensity are composed of frozen ice cloud particles. (They are called hot towers because their column of air is warmer than the surrounding air temperature, but above about 5-7 km to the tops of the towers at 15-19 km, the cloud particles are frozen.) This work showed that indeed, one can model information about cloud ice particle characteristics and indicated that non-spherical ice shapes, instead of spherical particles, provided the best match to the observations. Overall, this work shows that while non-spherical particles show promise, selecting and modeling a proper ice particle parameterization can be difficult and additional in situ measurements are needed to define and validate appropriate parameterizations. This work is important for developing Global Precipitation Measurement (GPM) mission satellite algorithms for the retrieval of ice characteristics both above the melting layer, as in Hurricane Erin, and for ice particles that reach the surface as falling snow.

Nonspherical and Spherical Characterization of Ice in Hurricane Erin for Wideband Passive Microwave Comparisons

Gail Skofronick-Jackson[1], Eric Holthaus[2], Cerese Albers[3], and Min-Jeong Kim[4]

1. NASA Goddard Space Flight Center, Greenbelt, MD
2. Columbia University, New York City, NY
3. Florida State University, Tallahassee, FL
4. NOAA, Camp Springs, MD

Corresponding Author: Gail Skofronick Jackson, Code 614.6, Building 33, Room A428, Greenbelt, MD 20771, 301-614-5720, FAX 301-614-5558, Gail.S.Jackson@nasa.gov

Significant Findings:

In order to better understand the characteristics and physical-to-radiative relationships of frozen hydrometeors in hurricane systems, computed brightness temperatures (T_B) from 10.7 to 183±10 GHz were compared with radiometric observations of Hurricane Erin (2001) from the NASA ER-2 aircraft. The focus was on the frozen particle microphysics and the high frequencies ($\geq$ 85 GHz) that are particularly sensitive to frozen particles. There were four significant findings. The first finding was that the MM5 cloud model did not have enough vertical resolution at its highest altitudes to produce the temperature profiles needed to compute T_B in the 55 to 60 GHz range and hence coincident dropsonde data was required. The second significant finding was the ocean surface conditions were difficult to ascertain in the hurricane eye so that brightness temperatures that depended on the surface conditions did not match the observations well. The third finding revealed the importance of the bulk asymmetry parameter (that describes the direction of scattering) in the resultant T_B values. Typically, passive remote sensing has attributed T_B values to the combination of the bulk absorption and scattering parameters, essentially ignoring the role of the asymmetry. The fourth and most important finding was that non-spherical particles, in this case modeled as bullet rosettes, provided the absorption, scattering, and asymmetry radiative properties that when used in the radiative transfer calculations gave the best match to the observations. Overall, this work shows that while non-spherical particles show promise, selecting and modeling a proper ice particle parameterization can be difficult and additional in situ measurements are needed to define and validate appropriate parameterizations. This work is important for developing Global Precipitation Measurement (GPM) mission satellite algorithms for the retrieval of ice characteristics both above the melting layer, as in Hurricane Erin, and for ice particles that reach the surface as falling snow.

Nonspherical and Spherical Characterization of Ice in Hurricane Erin for Wideband Passive Microwave Comparisons

Gail Skofronick-Jackson[1], Eric Holthaus[2], Cerese Albers[3], and Min-Jeong Kim[4]

1. NASA Goddard Space Flight Center, Greenbelt, MD
2. Columbia University, New York City, NY
3. Florida State University, Tallahassee, FL
4. NOAA, Camp Springs, MD

Corresponding Author: Gail Skofronick Jackson, Code 614.6, Building 33, Room A428, Greenbelt, MD 20771, 301-614-5720, FAX 301-614-5558, Gail.S.Jackson@nasa.gov

ABSTRACT:

In order to better understand the characteristics and physical-to-radiative relationships of frozen hydrometeors in hurricane systems, computed brightness temperatures (T_B) from 10.7 to 183±10 GHz were compared with radiometric observations of Hurricane Erin (2001) from the NASA ER-2 aircraft. The focus here is on the frozen particle microphysics and the high frequencies ($\geq$ 85 GHz) that are particularly sensitive to frozen particles. In order to initialize the cloud profiles used in the radiative transfer calculations, data from airborne radars, dropsondes, and cloud models were used. Three different ice parameterizations were used with these cloud profiles to obtain the particle radiative signatures: (1) a solid ice sphere, (2) a low ice density (fluffy) sphere, and (3) a non-spherical bullet rosette habit where the radiation attributes (scattering, absorption, and asymmetry properties) are computed using the Discrete Dipole Approximation. All low frequency calculations track the observations well except in the eye of Hurricane Erin where the surface wind speed and/or near surface temperatures were difficult to model. For the higher frequencies, the solid ice spheres produced T_{BS} that were too cold in most cases while the fluffy snow particle parameterizations produced T_{BS} that were much warmer than the observations. The comparisons between the calculated and observed T_{BS} show that in general the three dimensional rosette habit does the best job of matching the observations for most of the high frequencies because of its scattering and asymmetry parameters. Overall, this work shows that while non-spherical particles show promise, selecting and modeling a proper ice particle parameterization can be difficult and additional in situ measurements are needed to define and validate appropriate parameterizations.

Nonspherical and Spherical Characterization of Ice in Hurricane Erin for Wideband Passive Microwave Comparisons

Gail Skofronick-Jackson[1], Eric Holthaus[2], Cerese Albers[3], and Min-Jeong Kim[4]

1. NASA Goddard Space Flight Center, Greenbelt, MD

2. Columbia University, New York City, NY

3. Florida State University, Tallahassee, FL

4. NOAA, Camp Springs, MD

Corresponding Author: Gail Skofronick Jackson, Code 614.6, Building 33, Room A428, Greenbelt, MD 20771, 301-614-5720, FAX 301-614-5558, Gail.S.Jackson@nasa.gov

18   **ABSTRACT:**

19   In order to better understand the characteristics and physical-to-radiative

20   relationships of frozen hydrometeors in hurricane systems, computed brightness

21   temperatures (T_B) from 10.7 to 183±10 GHz were compared with radiometric

22   observations of Hurricane Erin (2001) from the NASA ER-2 aircraft. The focus here is

23   on the frozen particle microphysics and the high frequencies (≥ 85 GHz) that are

24   particularly sensitive to frozen particles. In order to initialize the cloud profiles used in

25   the radiative transfer calculations, data from airborne radars, dropsondes, and cloud

26   models were used. Three different ice parameterizations were used with these cloud

27   profiles to obtain the particle radiative signatures: (1) a solid ice sphere, (2) a low ice

28   density (fluffy) sphere, and (3) a non-spherical bullet rosette habit where the radiation

29   attributes (scattering, absorption, and asymmetry properties) are computed using the

30   Discrete Dipole Approximation. All low frequency calculations match the observations

31   reasonably well. For the higher frequencies, the solid ice spheres produced T_Bs that were

32   too cold in most cases while the fluffy snow particle parameterizations produced T_Bs that

33   were much warmer than the observations. The comparisons between the calculated and

34   observed T_Bs show that in general the three dimensional rosette habit does the best job of

35   matching the observations for most of the high frequencies primarily because of its

36   asymmetry coefficients. Overall, this work shows that while non-spherical particles show

37   promise, selecting and modeling a proper ice particle parameterization can be difficult

38   and additional in situ measurements are needed to define and validate appropriate

39   parameterizations.

1. Introduction

The development and strength of tropical cyclones is highly influenced by ice particles in hurricane rain bands and convection [e.g., *McFarquhar et al*, 2006; *Heymsfield et al*, 2006; *Willoughby*, 1998]. In fact "hot towers" associated with increasing hurricane intensity are composed of frozen ice cloud particles. (They are called hot towers because their column of air is slightly warmer than the surrounding air temperature, but above about 5-7 km to the tops of the towers at 15-19 km, the cloud particles are frozen.) However, little information is known about frozen droplet characteristics in hurricane clouds. While cloud resolving models do incorporate frozen particles [e.g., *Wu et al.*, 2006; *Tao et al.*, 2007], in general these modeled particles are only validated with extremely sparse in situ measurements or through comparisons between forward radiative transfer calculations using the model data and radiometer observations at frequencies up to 90 GHz. Unfortunately, the brightness temperature sensitivity to ice particles in clouds is limited by the physical and dielectric characteristics of ice for frequencies below 89 GHz. The sensitivity of higher frequency channels (> 100 GHz) to frozen particles has been proven [e.g., *Skofronick-Jackson et al.*, 2004; *Bennartz and Bauer*, 2003]. Without these higher frequencies the relationships between wide-band radiometer observations and the physical and electromagnetic properties of frozen hydrometeors cannot be determined or adequately retrieved. Understanding these physical-radiative relationships is important for developing Global Precipitation Measurement (GPM) mission satellite algorithms for the retrieval of ice characteristics both above the melting layer, as in Hurricane Erin, and for ice particles that reach the surface as falling snow.

2

63   The microphysical characteristics and high frequency radiative properties of

64   frozen particles are complex and difficult to ascertain without detailed in situ data sets. In

65   and above the melting layer frozen particles can range from spherical to nonspherical

66   habits and with multiple mixtures of ice, air, and water in a single particle. The

67   methodologies for determining the single particle and bulk layer radiative properties of

68   frozen particles rely on several assumptions and require computationally intensive

69   numerical models. In the past, many investigators assumed spherical particles in order to

70   reduce modeling complexities. More recently, the radiative properties for non-spherical

71   ice particles are being determined using the discrete dipole approximation [e.g., *Draine*

72   *and Flatau*, 1994; *Liu* 2004; *Kim*, 2006] and other models [e.g., *Xu and Gustafson*, 2001].

73   The Fourth Convection and Moisture Experiment (CAMEX-4) provides a

74   valuable database of active, passive, and in situ observations that is used to investigate

75   the relationships between frozen particles and their radiative signatures. The CAMEX-4

76   field campaign was based in Jacksonville, Florida during August and September of 2001

77   [*Kakar et al.*, 2006]. This field campaign was a joint NASA and NOAA Hurricane

78   Research Division project with the goal of studying tropical hurricane development,

79   tracking, intensification, and land falling impacts. While remote sensing of the hurricane

80   environment was the primary objective of CAMEX-4, there were also separate flights to

81   study thunderstorm structure, precipitation systems, and atmospheric water vapor

82   profiles. Multiple instruments located on ground, on low and high altitude aircraft, and

83   on satellites were used to observe convective and hurricane systems. Of particular interest

84   for this work are measurements from instruments on the high-altitude ER-2 aircraft at a

85   ~20 km altitude that provide a single active radar channel and 19 passive microwave

3

86   brightness temperature channels ranging from 10.7 to 183.31±10 GHz during Hurricane

87   Erin on 10 September 2001. The higher frequency channels are extremely useful for

88   determining and constraining the particle size distributions of the frozen hydrometeors

89   [*Skofronick-Jackson et al.*, 2003].

90   The purpose of this research is to compare observed brightness temperatures to

91   calculated brightness temperatures for several spherical and non-spherical frozen cloud

92   hydrometeor habits in order to study how the selected ice parameterizations affect the

93   radiative properties and resultant brightness temperatures. A radiative transfer model is

94   employed to convert the hydrometeor parameterizations into brightness temperature

95   values. The cloud profiles will be initialized with radar data through a conversion from

96   reflectivity to hydrometeor content values. Other initialization procedures include

97   determining boundary conditions and profile environmental conditions (e.g., surface wind

98   speed and temperature, pressure, and relative humidity profiles) using dropsondes from

99   the ER-2 and modeled Hurricane Erin data. The hydrometeor parameterizations (habits

100   and particle size distributions for the frozen droplets) are used to compute radiative

101   properties (absorption, scattering, and asymmetry) that are required for use in radiative

102   transfer calculations. Then the effects of these parameterizations on the computed

103   brightness temperatures (T_B) are compared to the observed T_B.

104   In section 2, details of the instruments and how the observations were co-located

105   will be provided. The generation of the cloud hydrometeor profiles and initialization of

106   boundary conditions will be described in Section 3. In Section 4 the radiative transfer

107   model used in the brightness temperature calculations is summarized along with the

108   radiative properties for each of the parameters. The comparisons between computed and

109   observed brightness temperatures are analyzed in Section 5, followed by a summary and

110   discussion of the key points in Section 6.

111

112   **2. Observations:**

113   While CAMEX-4 had broad-based instrumentation on multiple platforms

114   including several aircraft and ground locations, this work focuses on the observations

115   from four instruments on the ER-2 aircraft. On board the ER-2, flying at an altitude of

116   approximately 20 km, the instruments of interest for this work are the High Altitude

117   Monolithic Microwave Integrated Circuit (MMIC) Scanning Radiometer (HAMSR)

118   [*Lambrigtsen and Riley*, 2002], the Advanced Microwave Precipitation Radiometer

119   (AMPR) [*Spencer*, 1994], the ER-2 Doppler Radar (EDOP) [*Heymsfield et al.*, 1996],

120   and the ER-2 dropsonde system [*Halverson, et al.*, 2004]. The first three instruments

121   measure atmospheric hydrometeors in the microwave region of the electromagnetic

122   spectrum, while the dropsondes are released from the ER-2 and measure temperature,

123   relative humidity and wind speed in situ as they fall toward the Earth's surface. The

124   HAMSR has 8 observations between 50 and 57 GHz, plus 166, 183.3±1, 183.3±1.8,

125   183.3±3, 183.3±4.5, 183.3±7, and 183.3±10 GHz, while the AMPR observes at the lower

126   frequencies of 10.7, 19.35, 37, and 85.5 GHz. The EDOP is an active radar sampling at

127   9.6 GHz with a vertical range gate interval of 37.5 meters. HAMSR, AMPR, and EDOP

128   are cross-track scanning instruments.

129   The focus is on the rain bands and anvil regions associated with Hurricane Erin on

130   10 September 2001. As with many Atlantic tropical cyclones, Hurricane Erin can be

131   traced back to a tropical wave from western Africa starting 30 August 2001. Erin

132   continued to strengthen and became a hurricane by 0000 UTC 9 September, reaching its

133   peak intensity near 0000 UTC 10 September. On 10 September, the vertical wind shear

134   peaked and Erin began moving over cooler waters. In response, Erin began to weaken.

135   By 0000 UTC 15 September, Erin had turned into a tropical storm and eventually

136   transitioned into an extratropical system. The GOES satellite image of Hurricane Erin is

137   provided in Fig. 1 with the ER-2 aircraft flight line superimposed on top of it. The portion

138   of the ER-2 flight line investigated in this work is identified by a thick white line in Fig.

139   1. The flight line begins at 33.9 N, 66.14 W and goes to 37.22 N, 63.64 W in a straight

140   line and extends over about 450 km. Only the nadir or near-nadir signatures are used in

141   this analysis. Figure 1 also indicates the location of dropsonde releases from the ER-2

142   aircraft. These were the first successful dropsonde releases from a high altitude aircraft in

143   a hurricane [*Halverson, et al.*, 2006].

144   The CAMEX-4 instrument set did include the capability to measure habits and

145   PSDs in situ. Such instruments were flown on the DC-8 aircraft with a maximum altitude

146   of ~12 km. The in situ particle sampling instruments only obtain PSDs at the altitude of

147   the DC-8 aircraft and spirals of the aircraft are required to get PSDs over the vertical

148   space of the cloud. While CAMEX-4 had a few coordinated ER-2 overpasses of the DC-8

149   spiraling through convective clouds, unfortunately this did not occur on the 10 September

150   2001 flights for Hurricane Erin.

151   Figure 2 shows the EDOP, HAMSR, and AMPR observed data for Hurricane Erin

152   on 10 September 2001 between 16:49:59 UTC and 17:25:00 UTC, including EDOP data

153   (upper panel), selected HAMSR brightness temperatures (two center panels), and AMPR

154   brightness temperatures (lower panel). For this image, the ER-2 is flying toward the

155   northeast as indicated in Fig. 1. In the image the hurricane eye is surrounded by several

156   rain bands with anvil, convective, and stratiform regions. From Fig. 2, it can be discerned

157   that the higher frequencies of the HAMSR data ($\geq$ 166 GHz) are sensitive to the frozen

158   particles in the cloud (as indicated by non-zero reflectivities above the melting layer in

159   the EDOP image collocated with depressions in the brightness temperatures at 166 and

160   183 GHz). On the other hand, the AMPR lower frequency channels are sensitive to the

161   liquid in the rain bands. Although not readily apparent in Fig. 2, the HAMSR 50-60 GHz

162   channels are mostly sensitive to the temperature profile.

163   The data sets from the AMPR, HAMSR, and EDOP have been analyzed and

164   collocated. The largest footprint of 2.8 km occurs for the AMPR 10 and 19 GHz channels

165   at nadir when the ER-2 is flying at 20 km altitude. Because there is not an AMPR pixel

166   directly at nadir, the two pixels adjacent to nadir were averaged to simulate a nadir value.

167   The HAMSR footprint resolution is about 2.0 km at nadir. However, the HAMSR data

168   samples were separated by about 12 seconds, therefore the footprint centers were

169   separated by about 2.5 km based on a 205 m s^{-1} aircraft speed. Since the HAMSR and

170   AMPR footprint resolutions and locations are so similar, the collocation process was

171   simplified. Thus, AMPR, HAMSR, and closest EDOP times were matched to the 183

172   points in the HAMSR data over this flight time.

173

174   **3. Cloud Profile Initialization**

175   Prior to computing brightness temperatures for these 183 observational data

176   points, a cloud profile data set must first be generated. The radar reflectivity can provide

177   some information about the hydrometeors, however additional data about the atmospheric

178   profile and boundary conditions are required. There are three steps: (1) the EDOP radar

179   reflectivities are converted into vertical hydrometeor content profiles, (2) the temperature,

180   pressure, and relative humidity profiles need to be determined, and (3) the boundary

181   conditions for the ocean surface and top of atmosphere must be assigned. In order to

182   obtain the required information for steps 2 and 3, dropsonde and hurricane model data is

183   used. The role of the dropsondes is to provide detailed information about the temperature

184   and relative humidity profiles that is not adequately generated by the simulated Hurricane

185   Erin.

186   3.1 Hydrometeor Content Profiles

187   Attenuation corrected [*Hitschfeld and Borden*, 1954] nadir-viewed EDOP radar

188   reflectivity profiles are converted into estimates of hydrometeor content profiles. The fine

189   (37.5 m) resolution of the radar range gates from 0 to ~18 km is averaged to 0.25 km

190   vertical slabs. The hydrometeor content profiles from the radar-to-microphysical profile

191   algorithm are partitioned into liquid and frozen particles with exponential drop size

192   distributions, respectively. While continuity of the precipitation flux across the freezing

193   level is not explicitly enforced, the masses obtained from the radar reflectivities have

194   smooth transitions from one level to the next.

195   The averaged reflectivities are converted to rain rate using the *Marshall and*

196   *Palmer* [1948] relationship:

197    $$M_L(m,h) = 0.0055(Z_{obs}(m.h))^{0.55} \text{ g m}^{-3} \tag{1}$$

198   where M_L is the mass content of the liquid particles at the flight pixel m and height level h

199   associated with the attenuated corrected EDOP reflectivity Z_{obs} (in $\text{mm}^6 \text{ m}^{-3}$). Once the

200   temperature in the vertical profile reaches $0°$ C a portion of the content derived from Z_{obs}

201 is reserved for frozen particles. A linear interpolation is used to transition to all frozen

202 hydrometeors at $-22.5°$ C and colder. The conversion from reflectivity to frozen

203 hydrometeor content at each level is defined by the *Sekhon and Srivastava* [1970] particle

204 size distribution as follows:

205 $$M_F\ (m,h) = 0.0136\ (4.46\ Z_{obs}(m.h))^{0.39}\ \text{g m}^{-3} \tag{2}$$

206 where M_F is the mass content of the frozen particles and the 4.46 factor is a correction for

207 the frozen versus liquid particle refractive index that is usually stated as a 6.5 dBZ

208 addition to the observed reflectivity in dBZ [*Smith*, 1984]. The transformation from

209 reflectivities to particle contents populates the liquid and frozen hydrometeor vertical

210 profiles.

211   <u>3.2 Atmospheric Profiles</u>

212   Without temperature (T), pressure (P), and relative humidity (RH) profiles,

213 radiative transfer calculations cannot be performed. Simulated cloud fields from the

214 Mesoscale Model-5 (MM5) of Hurricane Erin [*Wu et al.*, 2006] were used in this analysis

215 to help generate atmospheric profiles. The MM5 model integration begins at 0000 UTC 7

216 September when Erin was an area of disturbed weather and was developed with a

217 resolution of 2.0 km horizontally and ranges between 0.004 and 1.0 km vertically. The

218 MM5 time step closest to the 10 Sept. 2001 at 1700 UTC time is selected for use within

219 this work. The rain rate statistics of the MM5 data (without zero values included) and

220 vertically summed liquid and frozen particle concentrations are provided in Table 1. In

221 order to extract appropriate T, P, and RH profiles, the MM5 computed reflectivity

222 profiles (Z_{sim}) generated by the model were compared to each of the EDOP reflectivity

223 profiles (Z_{obs}) to generate error values (E):

9

$$224 \qquad E(m) = \sum_{h=o}^{cldtop} \left| Z_{sim}(i,j,h) - Z_{obs}(m,h) \right| \qquad (3)$$

225 where m represents the mth of 183 profiles in the flight line, h is an index to the vertical

226 profile, and i, j are indices to the MM5 output. The i, j indices associated with the five

227 most minimum values of E for each m are used to average T and RH profiles of these five

228 MM5 profiles for use in the radiative transfer (RT) calculations.

229   When these MM5 derived T and RH profiles were used in RT calculations of

230 Hurricane Erin it became apparent that the modeled T profile at the upper altitudes was

231 not appropriate. This was determined by reviewing the 55.5 GHz T_B channel that is

232 sensitive to only the upper altitude temperatures. Figure 2 shows that the 55.5 GHz

233 observations are relatively steady across the varying cloud conditions over the flight line.

234 The computations using the MM5 generated T profiles were uniformly warm by about

235 5K. The inconsistency between the computed T_B using the MM5 T profile and the

236 observations is likely attributable to the coarser vertical resolution for MM5 profiles

237 above 300mb [*Wu et al.*, 2006]. When the MM5 temperature profiles are allowed to

238 transition to an average (16:47:56 and 17:31:05 UTC) dropsonde profile between 7 to 18

239 km instead of using the MM5 temperature profiles, the comparison is much better as will

240 be shown in Section 5. The problems in getting the calculations of 55.5 GHz to match the

241 observations indicate a disconnect between models and observations. Furthermore, in the

242 hurricane eye only, comparisons with the clear air 10 GHz T_B observed and computed

243 indicated consistently too cold (MM5) computed T_B. In order to compensate for the RH

244 and cloud water, data from dropsonde closest to the eye (1704 UTC) was employed for

245 the temperature, pressure, and relative humidity in the first 7 km nearest the surface.

246

247   3.3 Boundary Conditions

248   The final step is to insert boundary conditions. For the boundary conditions at the

249   top of the profile, the maximum height level is 18 km near the ER-2 flight altitude.

250   Radiation from the cosmic background is incorporated in the radiative transfer

251   calculations so that the effects of scattering from the ice at the top of the clouds are

252   included. At the Earth's boundary an oceanic surface is assumed since the flight leg is

253   over ocean during the focus times. The RT model requires ocean emissivity and

254   temperature. The ocean temperature was obtained by merging dropsonde and MM5 data.

255   Surface emissivity was more difficult to obtain since it is a function of surface roughness.

256   The average windspeeds emanating from the MM5 data as determined by Eqn. 3 were

257   found to be too weak to produce breaking waves with enough foam to increase emissivity

258   and T_B warming even though Table 1 shows a maximum windspeed of 44 m s^{-1}. This

259   discrepancy was determined using the 10 GHz channel that is sensitive to surface

260   conditions in clear air regions. The dropsonde windspeeds were greater than those of the

261   MM5 model and thus a linear fit between the values of the dropsonde were used, with a

262   minimum of 8 m s^{-1} in the eye. Using the dropsonde data the windspeeds started at 20 m

263   s^{-1} on the left hand side of the flight path, peaked at 40 m s^{-1} at the left side of the eye,

264   dropped to 8 m s^{-1} in the eye, peaked back to 50 m s^{-1} on the right edge of the eye wall,

265   and then transitioned to 10 m s^{-1} on the rightmost edge of the flight path. The *Monohan*

266   *and Woolf* [1989] static foam model worked best in generating realistic foam amounts for

267   ocean surface emissivity computations.

268

11

4. Particle Habit and Parameterizations

269   **4. Particle Habit and Parameterizations**

270   The frozen cloud particle contents (in g m^{-3}) derived from the EDOP reflectivities

271   are partitioned into three different frozen habits and exponential particle size distributions

272   (PSDs) in order to compute the electromagnetic absorption, scattering, and symmetry

273   factors of the frozen particles required for brightness temperature computations. These

274   factors describe how the incident radiation will be absorbed and scattered. The emissive

275   properties of the ocean surface and raindrops are also incorporated. The first habit uses

276   the solid spherical ice *Sehkon and Srivastava* [1970] PSD, while the second habit

277   assumes a dry fluffy spherical snow particle. The third parameterization assumes a three

278   dimensional bullet rosette of three columns intersecting at orthogonal angles at their

279   center points, like an X-Y-Z axis intersection. The *Marshall-Palmer* [1948] remains

280   constant as the liquid PSD for all three frozen habit cases.

281   Since detailed in situ habits and PSDs were not measured for this CAMEX-4 ER-

282   2 flight, the three frozen habits and PSD (or microphysical) parameterizations were

283   selected from published literature in order to compare how changes in the PSD and habit

284   for frozen hydrometeors affect the computed T_B and the comparison with the observed

285   T_B. While this is a qualitative comparison it still reveals information about the

286   applicability of the different frozen parameterizations with respect to the CAMEX-4

287   Hurricane Erin observations and different portions of the storm.

288   All of the three frozen habits employ polydispersive particle size distributions.

289   The absorption and scattering coefficients for each layer and hydrometeor are determined

290   by integrating over the polydispersive particle size distributions. For all

291   parameterizations, the PSD, or number density of the particles within the diameter range

292   D to $D + dD$, is modeled by a decaying inverse exponential function:

293                                $N(D) = N_0 \exp(-\Lambda D)$ (4)

294   where N_0 is a multiplier in $\text{m}^{-3}\text{mm}^{-1}$ and $\Lambda=(2<r>)^{-1}$ in mm describes the average radius

295   size parameter. At each height interval, the relationship between the bulk (summed)

296   scattering coefficient and bulk absorption coefficient can be used to indicate if radiative

297   cooling from scattering or warming from absorption will dominate. The asymmetry factor

298   describes the direction(s) of scattering with values close to $+1$ indicating forward

299   scattering, those close to -1 backward scattering, and those at zero indicating isotropic

300   scattering.

301   <u>4.1 Parameterization 1</u>

302   Here the frozen droplets use a fluffy particle PSD [*Tao and Simpson*, 1993]. The

303   particles are assumed to be 10% ice and 90% air with

304                           $N_{0fluffy} = 4000.0 \text{ m}^{-3} \text{ mm}^{-1}$ (5)

305                           $\Lambda^{-1}_{fluffy} = \dfrac{M}{\pi \rho_{fluffy} N_{0\,fluffy}} \text{ mm}$ (6)

306   where $\rho_{fluffy} = 0.1 \times 10^6 \text{ g m}^{-3}$ for 10% ice. The particles are spherical in shape. The

307   Maxwell-Garnett [*Bohren and Battan*, 1980] dielectric mixing theory is used to obtain

308   the refractive index of these mixed phase (ice and air) particles and then Mie theory is

309   used to determine the absorption, scattering, and asymmetry factors for the RT

310   computations. The particles are allowed to extend to a maximum size of about 10 mm

311   with N(D) on the order of 10^{-1} at this maximum size and for $M = 1 \text{ g m}^{-3}$.

312

313   4.2 <u>Parameterization 2</u>

314   For the second parameterization, the frozen drops follow that of the *Sehkon-*

315   *Srivastava* [1970] PSD, denoted SS. The SS PSD assumes solid ice spheres for the frozen

316   droplets. These were the size distributions used in Equation 2 to convert reflectivity to

317   hydrometeor ice content. The Λ and N_0 in Eqn. 4 are:

318     $$N_{0SS} = 636.38\, M^{1.093}\ \text{m}^{-3}\ \text{mm}^{-1} \tag{7}$$

319     $$\Lambda_{SS}^{-1} = 1.185\, M^{-0.524}\ \text{mm} \tag{8}$$

320   where M is the ice content in g m^{-3} in each cloud layer interval. The refractive index for

321   solid ice [*Warren*, 1984] is used in the Mie expressions for determining the radiative

322   properties. In the PSD the maximum size is 10 mm where the N(D) is 10^{-2} for M values

323   of 1.0 g m^{-3}.

324

325   <u>4.3 Parameterization 3</u>

326   This third parameterization has a habit similar to a bullet rosette with three

327   cylinders intersecting at their center points and is denoted C3. This habit was described in

328   *Kim* [2006], with the single cylinder aspect ratio from *Auer and Veal* [1970] and *Kim et*

329   *al.* [2007]:

330     $$D = 0.197L^{0.414}\ \text{(mm)} \tag{9}$$

331   where L is the length and D is the diameter of the column. The Λ in Eqn. 4 is a function

332   of the temperature as it varies over the profile height and comes from *Lo and Passarelli*

333   [1982]:

334     $$\Lambda_{C3}^{-1} = 10^{-T/41} \tag{10}$$

335   where T is in Celsius. The maximum size of the particle size distribution is fixed by Kim

336   2006 requiring that the size parameter ($\pi D_{eff}\, \lambda^{-1}$) < 2.5 where λ is the operational

337   wavelength and D_{eff} which is the effective diameter of a spherical particle with volume

338   given by the three intersecting cylinders. Note that we plotted *Kim's* [2006] provided

339   curve fits and determined that they were good up to size parameters of 3.5. Thus the

340   maximum L for this PSD is 7 mm. At 7 mm the N(D) value is on the order of 10^{-4}, while

341   for 5 mm N(D) is closer to 10^{-2} for T = -20°C and M = 1 g m^{-3}.

342   The volume for the 3 cylinder habit is given by:

343
$$V = \frac{3}{4}\pi D^2 L - \sqrt{2}D^3 \qquad (11)$$

344   where the intersecting center volume is removed for two of the cylinders. The A_{C3} is

345   determined using Eqn. (10). The habit shape and aspect ratio fixes the volume in each

346   individual particle such that given the maximum diameter the total ice water content (M)

347   in each layer can be partitioned into an exponential particle size distribution and N_0 can

348   be determined using Eqn (11). The increment in the L dimension for the particle size

349   distribution is 0.1 mm.

350   In order to compute the absorption, scattering, and asymmetry parameters for

351   these non-spherical particles, Mie theory is used for frequencies less than 80 GHz [*Kim,*

352   *2006*]. For frequencies above 80 GHz, the discrete dipole approximation is used [*Draine*

353   *and Flatau*, 1994]. The procedure is similar to that described in *Kim* [2006] and the DDA

354   curve fit coefficients for this aspect ratio are provided in Table 2. The curve fit equations

355   are from *Kim* [2006] and are reproduced here:

356
$$\log_{10}\left(\frac{C_{scat}}{\pi r_{eff}^2}\right) = \sum_{n=0}^{7} A_n \left(\log_{10} x\right)^n \qquad (12)$$

357

358
$$\frac{C_{abs}}{\pi r_{eff}^2} = \sum_{n=0}^{5} B_n x^n \qquad (13)$$

359

360
$$\log_{10}(g) = \sum F_n (\log_{10} x)^n . \qquad (14)$$

361   To provide proper disclosure, the resultant brightness temperatures are relatively

362   sensitive to the habit and the prescribed PSD. For example, a single column habit

363   produced warmer brightness temperatures than this three intersecting column habit.

364   Further, changing the aspect ratio of the individual columns does affect the radiative

365   properties. Finally, we have imposed a PSD [*Lo and Passarelli*, 1982] though we have

366   noted that changing the $\Lambda(T)$ will affect the brightness temperatures as well.

367

368   **5. Radiative Transfer Calculations**

369   An accurate and efficient radiative transfer (RT) model is required to transform

370   the microphysical information into upwelling passive microwave brightness temperatures

371   (T_B) that are then compared to the AMPR and HAMSR observations. The radiative

372   transfer model used in this work is a planer-stratified scattering based model originally

373   developed by *Gasiewski* [1993] and modified as described in *Skofronick-Jackson et al.*,

374   [2003]. The RT model used herein allows for multiple scattering among the six different

375   hydrometeor types (i.e., suspended cloud water, rain, suspended cloud ice, snow, hail,

376   and graupel). In this work only rain and snow are allowed, though the size distributions

377   for rain and snow extend down to sizes appropriate for cloud water and cloud ice.

378   Flexibility exists in that the user can select observation height, viewing angle, frequency

16

379 (tested from 6 to 425 GHz) and polarization. The RT model requires as input instrument

380 specifications, vertical profiles of temperature, height, relative humidity, and PSDs of the

381 hydrometeors in the cloud or their radiative properties. It is assumed that a planar

382 stratified RT model is acceptable in this work since only high resolution nadir

383 observations are used in the retrieval. Furthermore, since only nadir observations are

384 analyzed in this work, any polarization sensitivity due to nonspherical particles is

385 minimized.

386   Once individual absorption, scattering, and asymmetry factors have been

387 computed for each shape as described in Section 4, they are integrated over

388 polydispersive PSDs as described in *Gasiewski* [1993] to obtain the bulk absorption,

389 scattering, and asymmetry factors over the vertical structure of the hurricane flight line.

390 Figure 3 shows the bulk absorption coefficients for the three different frozen habits at

391 183 ± 7 GHz, while Figure 4 provides the scattering coefficients. There is essentially no

392 difference in the absorption profiles since the Marshall-Palmer PSD for rain was not

393 changed and ice particle do not contribute much to the absorption coefficient. For the

394 scattering profiles, the fluffy and rosette habits tend to produce a bit more scattering than

395 the SS case. Scattering is increased for the fluffy by its relatively large particle size and

396 larger N(D) at those larger sizes. For the rosette habit, scattering is larger than that of the

397 SS particles but less than that of the fluffy particles because of its intermediate size and

398 N(D) values.

399   On the other hand, the asymmetry parameters at 183 ± 7 GHz (and for each

400 frequency in turn) are very different for the three cases (Figure 5). For fluffy spheres, the

401 asymmetry is above 0.8 for the highest altitudes (Fig. 5a) and closer to 0.5 in the mid-

402 altitude range. For the solid ice sphere (SS) case, the asymmetry factors are near 0.4 to

403 0.6 in most of the liquid and frozen parts of the vertical profile. On the other hand, the

404 three-dimensional rosette particle has asymmetry values decreasing with altitude (Fig.

405 5c). Since an asymmetry factor of +1.0 is pure forward scattering, the fluffy spheres

406 allow the warm emission from rain and the Earth's surface to forward scatter into the

407 radiometer and the cold cosmic background to forward scatter to lower layers, hence

408 producing warmer brightness temperatures. For the SS shapes, the asymmetry factor

409 shows a slight preference for forward scattering, but a bit more isotropic. Thus because of

410 multiple scattering effects, radiation is scattered such that the resulting effect for the SS

411 shape is cold brightness temperatures. Finally, for the three-dimensional rosette particles,

412 the asymmetry factor is similar to the asymmetry of the SS particles except that it goes to

413 close to zero at the top of the cloud. This is because Λ_{C3} is a function of temperature and

414 hence so is the average particle size at each temperature layer. This means that at the top

415 of the cloud, where the radiometer will receive most of the signal, particles are small and

416 scattering is isotropic, so the radiometer senses both warming from rain and/or surface

417 emission and cooling from cold cosmic background and the upper cloud layers. Because

418 the cold upper layers are closer to the radiometer, they have a larger impact in cooling the

419 radiometer brightness temperatures.

420 At 85 GHz, the absorption fields for the three parameterizations are as equivalent

421 as in the 183 GHz case. On the other hand the scattering profiles (Fig. 6) show that only

422 the SS parameterization has significant scattering in the ice layers. In Fig. 7, the 85 GHz

423 asymmetry shows a pattern similar to the 183 GHz asymmetry but at lower and more

424 isotropic values.

425   Although not shown, for 166 GHz the absorption, scattering, and asymmetry

426   factors have similar patterns as at 183 GHz. At 10 GHz the asymmetry factor ranges

427   between -0.05 and 0.2 for all three frozen habits. This means that any 10 GHz scattering

428   (also less than ~0.25 neper km^{-1} for all habits) is more isotropic, however at 10 GHz the

429   strong absorption coefficient overpowers the weak scattering signal.

430   **6. Comparison between Observed and Computed Brightness Temperatures**

431   The radiative transfer model along with the computed bulk radiative data were

432   used to compute brightness temperature values for the three ice parameterizations. These

433   values for many of the frequencies are presented in Figures 8, and 9. Prior to comparing

434   observations to the calculations, a review of Figure 2 will show that the cloud structures

435   are quite variable in several sections of the ER-2 flight line and these will cause some

436   discrepancies between the observations and the calculations in these regions since the

437   microphysical properties are apt to be quite variable as well. Specifically, time frames of

438   16:58 UTC through 17:04 UTC and about 17:15 UTC and 17:20 UTC near the transitions

439   between inner and outer hurricane rain bands are highly variable. Note that in the

440   hurricane eye all three parameterizations produce equivalent computed brightness

441   temperature values. This means that differences in T_B outside the eye are due to the

442   differences in the three frozen parameterizations.

443   In general, the fluffy particles did not produce enough scattering and proper

444   asymmetry directions to reduce calculated brightness temperatures to the lower observed

445   values at the higher frequencies. On the other hand, the solid ice sphere (SS) produced

446   excessive scattering in some locations. The three-dimensional rosettes managed to

447   reasonably capture the observed AMSR and HAMSR brightness temperatures. In the

19

448 following paragraphs the results for the different parameterizations will be discussed for

449 each plotted frequency.

450   For 10 GHz, all three parameterizations track the observations along the flight

451 line reasonably well and are within ~10K except in the eye of Hurricane Erin. While the

452 corrections in surface windspeed and near surface temperature and relative humidity

453 profiles did warm 10 GHz by ~10-20 K (see section 3.3), additional measures are

454 necessary. Perhaps wind driven foam persists even the calm of the eye. This is a future

455 research topic.

456   For 19 GHz, there is a similar response as for 10 GHz. For both 19 and 10 GHz,

457 brightness temperature calculations near the regions of a clearly defined radar bright band

458 (horizontal red lines in Figure 2, EDOP image) are depressed with respect to the

459 observations. This may indicate that the Marshall-Palmer PSD used for rain and/or the

460 vertical transitions between all rain and all ice are inadequately modeled. For 19 GHz

461 adding a melting layer would warm the T_B values by 2-3 Kelvin [*Skofronick-Jackson et*

462 *al.*, 2002].

463   For 37 GHz the calculations for all parameterizations track the observations,

464 except near the Hurricane Erin's eye (as for 10 and 19 GHz). There is more variability

465 among the three parameterizations since 37 GHz is sensitive to both ice and rain

466 particles. In this region, Hurricane Erin and the microphysical profile is complex with ice

467 aloft separated from rain below with clear air between. This type of cloud structure is

468 extremely difficult to appropriately model. For 37 GHz, adding a melting layer would

469 have the largest impact where T_B values are increased by up to 5-15 K [*Skofronick-*

470 *Jackson et al.*, 2002].

471   For 55.5 GHz the brightness temperatures do not change by more than 5-6 Kelvin

472   across the whole flight line observations due to the fact that this channel is sensitive to

473   temperatures high in the atmosphere, closest to the ER-2 aircraft. Since the sensitivity

474   altitude exists above any hydrometeors, there is little response of this channel to

475   hydrometeors. As noted in Section 3.2, the MM5 generated T profiles were replaced by

476   the colder profiles from the dropsondes. This was required to get the 55.5 GHz T_B

477   calculations closer to the observations.

478   For 85 GHz in Figure 8, brightness temperatures from the three parameterizations

479   show more deviations. This is expected since the three parameterizations differ only in

480   their frozen particle characteristics and 85 GHz is responsive to frozen hydrometeor

481   characteristics. Here the SS habit causes too much cooling due to high scattering and the

482   nature of its asymmetry factor. The fluffy particles have relatively low scattering and

483   high asymmetry such that warming from lower absorptive layers is reflected in the

484   warmer TB values. For the rosette particles, 85 GHz scattering is almost non-existent and

485   asymmetry is mostly isotropic (see Fig. 6 and 7), which means there is little contribution

486   of cooling from ice scattering at 85 GHz for the rosette particles. It is likely that adding a

487   melting layer would increase T_B values by ~5-10K [*Skofronick-Jackson et al.*, 2002]

488   which is the wrong direction of change if the goal is to cool calculations to match the

489   observations. The most likely cause of the discrepancy for the computed T_B with respect

490   to the observed T_B is that the rosette, fluffy, and SS particles are not typical particles that

491   exist at the mid-levels at 85 GHz senses. This means that the vertical distribution of PSDs

492   (and hence average particle size) is not yet appropriate for the mid-level particle that 85

493   GHz senses.

494   In the first panel of Figure 9, the 166 GHz channel image is shown. The 166 GHz

495   channel is a window channel like 85 GHz, however it responds to ice particles smaller

496   and at a higher altitude than those sensed by the 85 GHz channel due to its smaller

497   operating wavelength. For the 166 GHz channel, the rosette habit and its PSD produces a

498   better match to the observations than do the other parameterizations.

499   In Figure 9 some of the 183 GHz water vapor channel series of the HAMSR

500   instrument are shown. As the channels move from 183±1 to 183±10 GHz the sensitivity

501   moves from the top of the cloud to lower altitudes in the cloud. In the absence of clouds

502   these channels respond to the water vapor in clouds and are used to estimate water vapor

503   profiles. When clouds are present, these channels respond to the frozen hydrometeors

504   mostly, since these channels have a small operating wavelength and become saturated

505   quickly in the presence of particles with diameters near the operating wavelength.

506   In each of the comparisons between observation and calculations for the 183 GHz

507   channels, the best parameterization appears to be the one employing the C3 rosette

508   particles and the *Lo and Passarelli* [1982] PSD. The SS parameterization causes too

509   much scattering, while the fluffy particles do not provide enough scattering and proper

510   asymmetry directions at these higher frequencies.   The effective dielectric mixing

511   theories [*Bohren and Battan*, 1980] used for the fluffy particles assume that the size of

512   the inclusion is much smaller than the wavelength of the radiometer frequency [*Sihvola*,

513   1989]. Using these models for the higher frequencies seemed to produce inappropriate

514   electromagnetic characteristics. For example, the fluffy particles represented by effective

515   medium mixing models did not have cold enough T_B because the asymmetry factor was

516   too large. As stated previously, the asymmetry factor is a function of the particle shape,

22

517 size, temperature, and ice-air-water composition and determines the direction(s) of

518 scattering from a hydrometeor. Large asymmetry factors increased forward scattering of

519 the radiation from the warm lower layers so that computed brightness temperatures were

520 too warm. The C3 rosette shape along with the discrete dipole approximation along with

521 the *Lo and Passerelli* [1982] PSD produced the scattering and asymmetry factors that led

522 to the T_B computations closest to the observations.

523

524 **7. Summary and Conclusions**

525   This work was undertaken in order to evaluate the relationships between frozen

526 cloud particles and their radiative signatures for improving algorithm development of ice

527 particle characteristics (for falling snow retrievals and hurricane intensity assessments.)

528 In summary, three different ice parameterizations were used to compute brightness

529 temperature values to compare with observations from CAMEX-4 radiometers on the

530 ER-2 aircraft. In order to initialize the cloud profiles used in the radiative transfer

531 calculations, the radar reflectivities taken from the EDOP instrument on the ER-2 were

532 converted to mass contents at 0.25 km interval levels from 0.25 km to 18 km in the

533 vertical profile. The EDOP reflectivities were compared to Hurricane Erin MM5 modeled

534 reflectivities to extract and average the five closest atmospheric profiles such that the

535 MM5 profiles of temperature, pressure, and relative humidity were available across the

536 ER-2 flight path data set. Surface wind speeds and ocean surface temperature are

537 similarly generated. The MM5 generated temperature profiles above 7.5 km were

538 replaced by the dropsonde data due to coarse sampling in the upper altitude MM5

539 modeled profiles that caused inconsistencies in the frequency (55.5 GHz) sensitive to

23

540   high altitude temperature profiles. Surface windspeeds are similarly interpolated from the

541   dropsonde data.

542   With the profile database generated by the EDOP instrument, dropsondes, and the

543   Hurricane Erin MM5 model, brightness temperatures were computed for the three ice

544   parameterizations. The liquid drops followed the *Marshall and Palmer* [1948] PSD

545   throughout all parameterizations. The first parameterization relied on the *Sehkon and*

546   *Srivastava* [1970] PSD for ice particles, the second parameterization relied on fluffy

547   (10% ice, 90% air) particles, while the third parameterization was of a three-dimensional

548   bullet rosette particle of three intersecting cylinders in a polydispersive size distribution.

549   In comparing the observations to the calculations, the overall best fit resulted

550   from the rosette particles of three intersecting cylinders. The fluffy did not produce the

551   cold scattering signatures caused by ice that was measured in the observations. This

552   indicates inadequate modeling of its scattering and asymmetry electromagnetic

553   characteristics likely caused by representing them as fluffy, 10% ice spheres.

554   As would be expected, the lower frequency AMPR observations (10 to 19 GHz)

555   had essentially no difference among the three parameterizations (Figure 8). These

556   channels are mostly responsive to the liquid particles in the cloud and the

557   parameterizations discussed herein only made changes to the frozen droplets. At 37 GHz,

558   we expect and note a response to both liquid and frozen particles. The 50 to 60 GHz band

559   of the HAMSR instrument is typically used for temperature profiling with the lower

560   frequencies sensing more about the lower altitudes and vice-versa for the slightly higher

561   frequencies. These temperature profiling channels are responsive to hydrometeors in the

562   cloud except at the higher frequencies close to 60 GHz that sense only high altitude

563 atmospheric temperatures. The 183 GHz channels are sensitive to both atmospheric water

564 vapor and the frozen droplets in the cloud. The SS parameterization tended to

565 overemphasize the scattering and caused T_B that were too cool with respect to the

566 observations, while the bullet rosette (three cylinder) T_B values more closely match these

567 high frequency observations. Using rosette particles in the RT calculations matched all

568 frequencies except at 85 GHz where calculations were too warm. This is likely caused by

569 complex microphysical variations in the frozen particle habit and its PSD that is poorly

570 modeled across the vertical profile.

571   The four most significant findings of this work are summarized here. The first

572 finding was that the MM5 cloud model did not have enough vertical resolution at its

573 highest altitudes to produce the temperature profiles needed to compute T_B in the 55 to 60

574 GHz range and hence coincident dropsonde data was required. The second significant

575 finding was the ocean surface conditions were difficult to ascertain in the hurricane eye

576 so that brightness temperatures that depended on the surface conditions did not match the

577 observations well. The third finding revealed the importance of the bulk asymmetry

578 parameter (that describes the direction of scattering) in the resultant T_B values. Typically,

579 passive remote sensing has attributed T_B values to the combination of the bulk absorption

580 and scattering parameters, essentially ignoring the role of the asymmetry. The fourth and

581 most important finding was that non-spherical particles, in this case modeled as bullet

582 rosettes, provided the absorption, scattering, and asymmetry radiative properties that

583 when used in the radiative transfer calculations gave the best match to the observations.

584   This work has shown that the full channel spectrum of electromagnetic properties

585 of frozen hydrometeors is difficult to model using a single simplified parameterization

25

586 and that the bulk asymmetry factor plays a big role in the resultant computed high

587 frequency brightness temperatures. In likelihood, multiple habit and PSD models will be

588 required. These physical models will depend on many factors such as vertical location

589 and atmospheric temperature, method of forming and re-freezing, and ice-air-water

590 ratios. Detailed in situ observations and reliable cloud resolving models for the ice phase

591 particles are required in order to develop and validate appropriate and more universal

592 frozen particle parameterizations for radiative transfer calculations. Meanwhile this work

593 shows that some early non-spherical models such as the three-dimensional bullet rosette

594 with three intersecting cylinders can produce brightness temperatures comparable to most

595 wideband passive observations.

596

597 **Acknowledgments**

608
609
610
611
612 **References:**

613 Auer, A. H., and D. L. Veal (1970), The dimension of ice crystals in natural clouds, *J.*
614 *Amos. Sci.*, *27*, 919-926.
615
616 Bennartz, R. and P. Bauer (2003), Sensitivity of microwave radiances at 85 183 GHz to
617 precipitating ice particles, *Radio Science*, *38*(4), 8075, doi:10.1029/2002RS002626.
618

619   Bohren, C. F., and L. J. Battan (1980), Radar backscattering by inhomogeneous
620   precipitating particles. *J. Atm. Sci.*, *37*, 1821-1827.

621   Draine, B. T., and P. J. Flatau (1994), Discrete dipole approximation for scattering
622   calculations, *J. Opt. Soc. Am.*, *A11*, 1491-1499.
623

624   Gasiewski, A. J. (1993), Microwave radiative transfer in hydrometeors, in *Atmospheric*
625   *Remote Sensing by Microwave Radiometry*, edited by M. A. Janssen, pp. 91-144,
626   John Wiley and Sons.
627

628   Halverson, J.B., J. Simpson, G. Heymsfield, H. Pierce, T. Hock, and L. Ritchie (2006),
629   Warm core structure of Hurricane Erin diagnosed from high altitude dropsondes
630   during CAMEX-4, *J. Atmos. Sci.*, *63*, 309-324.
631

632   Heymsfield, G. M., S. Bidwell, I. J. Caylor, S. Ameen, S. Nicholson, W. Boncyk, L.
633   Miller, D. Vandemark, P. E. Racette, and L. R. Dod (1996), The EDOP radar system
634   on the high-altitude NASA ER-2 aircraft, *J. Atmos. Ocean. Tech., 13,* 795-809.
635

636   Heymsfield, A. J, A. Bansemer, S. L. Durden, R. L. Herman, and T. P. Bui (2006), Ice
637   microphysics observations in Hurricane Humberto: Comparison with non-hurricane
638   generated ice cloud layers, *J. Atmos. Sci.*, *63*, 288-308.
639

640   Hitschfeld, W. and J. Bordan (1954), Errors inherent in the radar measurement of rainfall
641   at attenuating wavelengths, *J. Meteor.*, *11*, 58-67.
642

643   Kakar, R., M. Goodman, R. Hood, and A. Guillory (2006), Overview of the Convection
644   and Moisture Experiment (CAMEX), *J. Atmos. Sci.*, *63*, 5-18.
645

646   Kim, M.-J. (2006), Single scattering parameters of randomly oriented snow particles at
647   microwave frequencies, *J. Geophys. Res.*, *111*, D14201, doi:10.1029/2005JD006892.
648

649   Kim, M.-J., J. A. Weinman, W. S. Olson, D.-E. Chang, G. Skofronick-Jackson, and J. R.
650   Wang (2007), A Physical Model to Estimate Snowfall over Land using AMSU-B
651   Observations, Submitted to *J. Geophys. Research*, March 2007.
652

653   Lambrigtsen, B. H. and A. L. Riley (2002), Microwave Scattering Observed in
654   Convective Cells During CAMEX-4. Proceedings AMS 25th Conference on
655   Hurricanes and Tropical Meteorology; San Diego, CA, 13A.6.
656

657   Liu, G. (2004), Approximation of single scattering properties of ice and snow particles
658   for high microwave frequencies, *J. Atmos. Sci.*, *61*, 2441 2456.
659

660   Lo, K. K. and R. E. Passarelli (1982), The growth of snow in winter storms: An airborne
661   observational study, *J. Atmos. Sci.*, *39*, 697-706.
662

663   Marshall, J. S. and W. M. Palmer (1948), The distribution of raindrops with size, *J.*
664   *Meteor.*, *5*, 165-166.

665

666   McFarquhar, G. M., H. Zhang, G. Heymsfield, R. Hood, J. Dudhia, J. B. Halverson, and
667   F. Marks Jr. (2004), Factors affecting the evolution of Hurricane Erin and the
668   distributions of hydrometeors: Role of microphysical processes. *J. Atmos. Sci.*, *63*,
669   127-150.

670

671   Monahan, E. C. and Woolf, D. K. (1989), "Comments on "Variations of Whitecap
672   Coverage with Wind Stress and Water Temperature" ", *J. Phys. Oceanogr. 19*, 706
673   709.

674

675   Sehkon, R. S. and R. Srivastava (1970), Snow size spectra and radar reflectivity, *J.*
676   *Atmos. Sci.*, *27*, 299-307.

677

678   Sihvola, A.H. (1989), Self-consistency aspects of dielectric mixing theories, *IEEE Trans.*
679   *on Geosci. and Remote Sens.*, *27*, 403-415.

680

681   G. M. Skofronick-Jackson, A. J. Gasiewski, and J.R. Wang, 2002: Influence of
682   microphysical cloud parameterizations on microwave brightness temperatures," *IEEE*
683   *Trans. Geosci. and Remote Sensing*, *40*, 187-196.

684

685   Skofronick-Jackson, G. M., M. J. Kim, J. A. Weinman, and D. E. Chang (2004), A
686   physical model to determine snowfall over land by microwave radiometry, *IEEE*
687   *Trans. Geosci. Remote Sens.*, *42*, 1047-1058.

688

689   Smith, P. L. (1984), Equivalent radar reflectivity factors for snow and ice particles, *J.*
690   *Clim. Appl. Meteorol.*, *23*, 1258-1260.

691

692   Spencer, R.W., R.E. Hood, F.J. LaFontaine, E.A. Smith, R. Platt, J. Galliano, V.L.
693   Griffin, and E. Lobl (1994), High-resolution imaging of rain systems with the
694   advanced microwave precipitation radiometer, *J. Atmos. Ocean. Tech.*, *11*, 849-857.
695   Tao, W.-K., J. Shi, S. Chen, S. Lang, S.-Y. Hong, C. Peters-Lidard, S. Braun, and J.
696   Simpson (2007), Revised bulk-microphysical schemes for studying precipitation
697   processes. Part I: Comparisons with other schemes, Submitted to *Mon. Wea. Rev.*
698   February 2007.

699

700   Tao, W.-K., and J. Simpson (1993), Goddard Cumulus Ensemble Model. Part I: Model
701   description, *Terrestrial, Atmospheric, and Oceanic Sciences*, *4*, 35-72.

702

703   Warren, S. G. (1984), Optical constants of ice from the ultraviolet to the microwave,
704   *Appl. Optics*, *23*, 1206 1225.

705

706   Willoughby, H.E. (1998), Tropical cyclone eye thermodynamics, *Mon. Wea. Rev.*, *126*,
707   3053-3067.

708

709   Wu, L., S. A. Braun, J. Halverson, G. Heymsfield (2006), A Numerical Study of
710   Hurricane Erin (2001). Part I: Model Verification and Storm Evolution, *J. Atmos.*
711   *Sci.*, *63*, 65-86.
712
713   Xu y.-L. and B.A.S, Gustafson (2001), A generalized multiparticle mie-solution: Further
714   experimental verification, *JQSRT, 70*, 395-419.

715   Figure Captions:

716   Figure 1: Visible GOES image with 10 September 2001 ER-2 aircraft flight track
717   superimposed. The flight line of interest in this work is identified with a thick white
718   line with an arrow showing flight direction. Stars indicate three dropsonde release
719   locations.
720

721   Figure 2: Collocated EDOP-HAMSR-AMPR Hurricane Erin data set from 10 September
722   2001.
723

724   Figure 3: Bulk absorption fields at 183 ± 7 GHz for (a) fluffy spheres, (b) solid ice SS
725   spheres, and (c) three-dimensional rosettes. Shading thresholds are at 0.1, 0.5, 1.0,
726   and 2.0 nepers/km.
727

728   Figure 4: Bulk scattering fields at 183 ± 7 GHz for (a) fluffy spheres, (b) solid ice SS
729   spheres, and (c) three-dimensional rosettes. Shading thresholds are at 0.1, 0.5, 1.0,
730   2.0, 3.0, and 4.0 nepers/km.
731

732   Figure 5: Bulk asymmetry fields at 183 ± 7 GHz for (a) fluffy spheres, (b) solid ice SS
733   spheres, and (c) three-dimensional rosettes. Asymmetry factors are unitless.
734

735   Figure 6: Bulk scattering fields at 85 GHz for (a) fluffy spheres, (b) solid ice SS spheres,
736   and (c) three-dimensional rosettes. Shading thresholds are at 0.1, 0.5, 1.0, 2.0, 3.0,
737   and 4.0 nepers/km.
738

739   Figure 7: Bulk asymmetry fields at 85 GHz for (a) fluffy spheres, (b) solid ice SS
740   spheres, and (c) three-dimensional rosettes. Asymmetry factors are unitless.
741

742   Figure 8: Brightness temperature values for 10, 19, 37, 55.5, and 85 GHz in Kelvin for
743   the observations (solid line), SS parameterization (dotted line), Fluffy
744   parameterization (dashed line), and rosette parameterization (dash-dotted line).
745

746   Figure 9: Same as Figure 6 except for 166, 183.3 ± 1, ±3, ±7, and ±10 GHz.
747

748

Field	Average	Median	Maximum
Surface Rain Rate (mm hr^{-1})	4.8	0.2	19.1
Liquid Profile Total (g m^{-3})	3.5	0.9	69.5
Ice Profile Total (g m^{-3})	1.6	0.5	36.1
Surface Wind Speeds (m s^{-1})	20.09	19.5	44.8

749   Table 1: MM5 Model statistics, zero values not included in average.

750

751

752

	Scattering Coefficient		Asymmetry Coefficient		Absorption Coefficient 85 GHz	Absorption Coefficient 166 GHz	Absorption Coefficient 183 GHz
A_0	-0.4732	F_0	-0.3464	B_0	1.5E-04	1.1E-04	-6.6E-04
A_1	2.7905	F_1	0.9238	B_1	0.0021	0.0061	0.0153
A_2	-0.7234	F_2	-1.9033	B_2	0.0081	0.0086	-0.0032
A_3	0.8752	F_3	1.5002	B_3	-0.0051	-0.0022	0.0062
A_4	-0.8767	F_4	2.7539	B_4	0.002	5.35E-4	-0.0014
A_5	-3.5739	F_5	-1.8551	B_5	-2.6E-04	-4.8E-05	8.5E-05
A_6	-2.6398	F_6	-3.6527	-	-	-	-
A_7	-0.6078	F_7	-1.2428	-	-	-	-

753   Table 2: Fitting Coefficients for equations 12, 13, and 14.

754

31

755
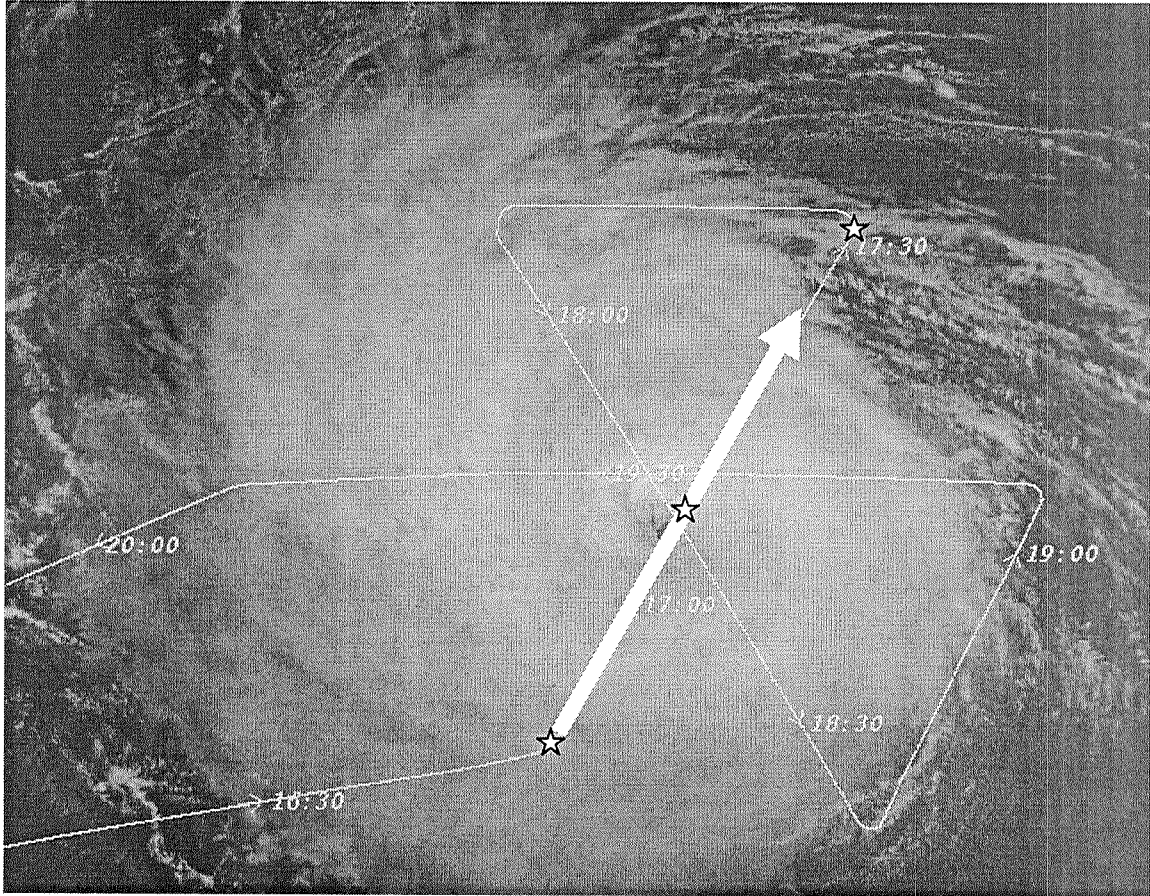
756
757
758 Figure 1: Visible GOES image for 10 September 2001 at 17:01 UTC with 10 September
759 2001 ER-2 aircraft flight track superimposed. The flight line of interest in this work is
760 identified with a thick white line with an arrow showing flight direction. Stars indicate
761 three dropsonde release locations.
762

Figure 2: Collocated EDOP-HAMSR-AMPR Hurricane Erin data set from 10 September 2001.
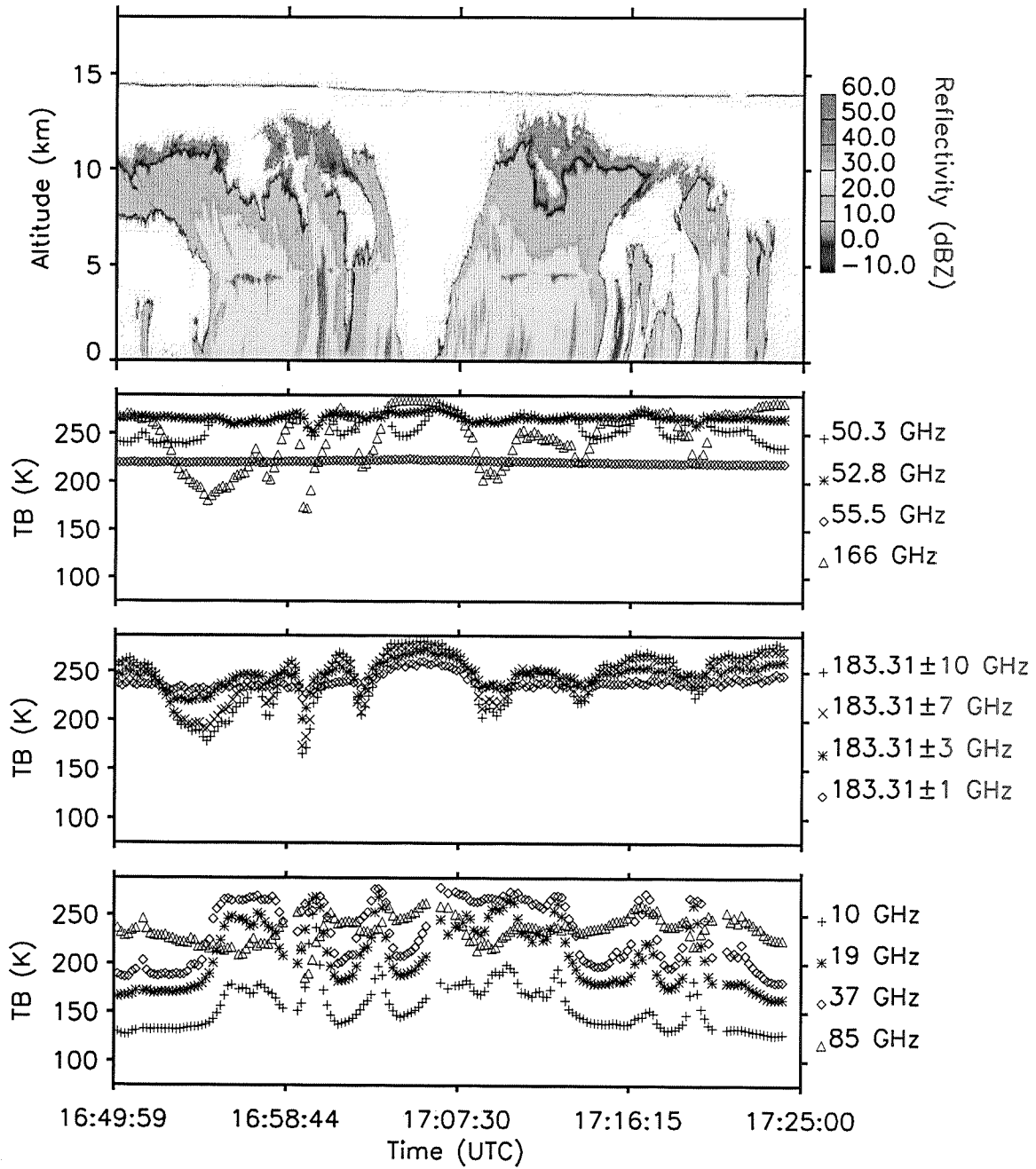
763
764
765
766
767
768
769
770
771
772
773
774

183 GHz Absorption

777 Figure 3: Bulk absorption fields at 183±7 GHz for (a) fluffy spheres, (b) solid ice SS
778 spheres, and (c) three-dimensional rosettes. Shading thresholds are at 0.1, 0.5, 1.0, and
779 2.0 nepers/km.
780
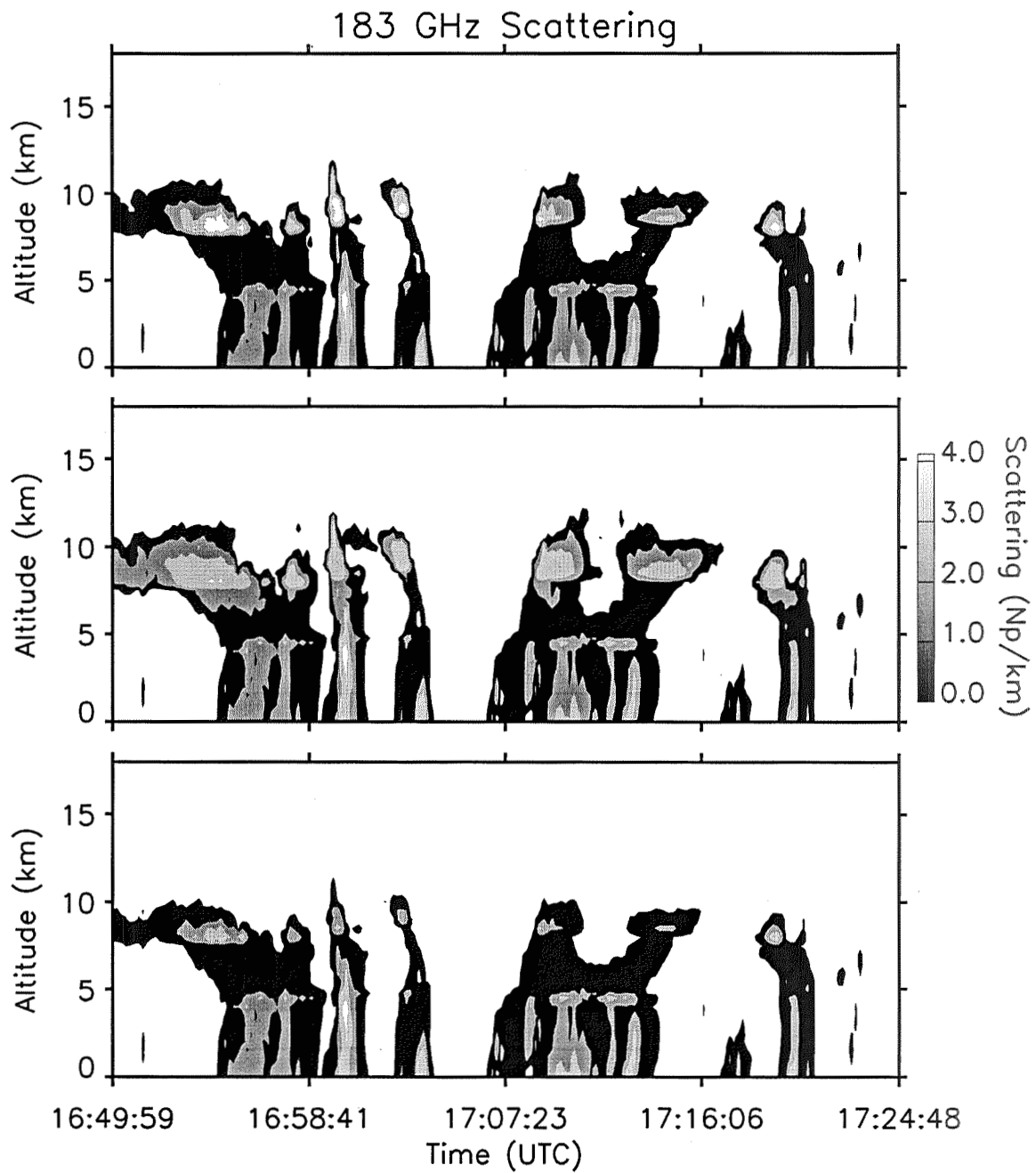
183 GHz Scattering

781
782
783 Figure 4: Bulk scattering fields at 183±7 GHz for (a) fluffy spheres, (b) solid ice SS
784 spheres, and (c) three-dimensional rosettes. Shading thresholds are at 0.1, 0.5, 1.0, 2.0,
785 3.0, and 4.0 nepers/km.
786
787
788
789

183 GHz Asymmetry

Figure 5: Bulk asymmetry fields at 183±7 GHz for (a) fluffy spheres, (b) solid ice SS spheres, and (c) three-dimensional rosettes. Asymmetry factors are unitless.
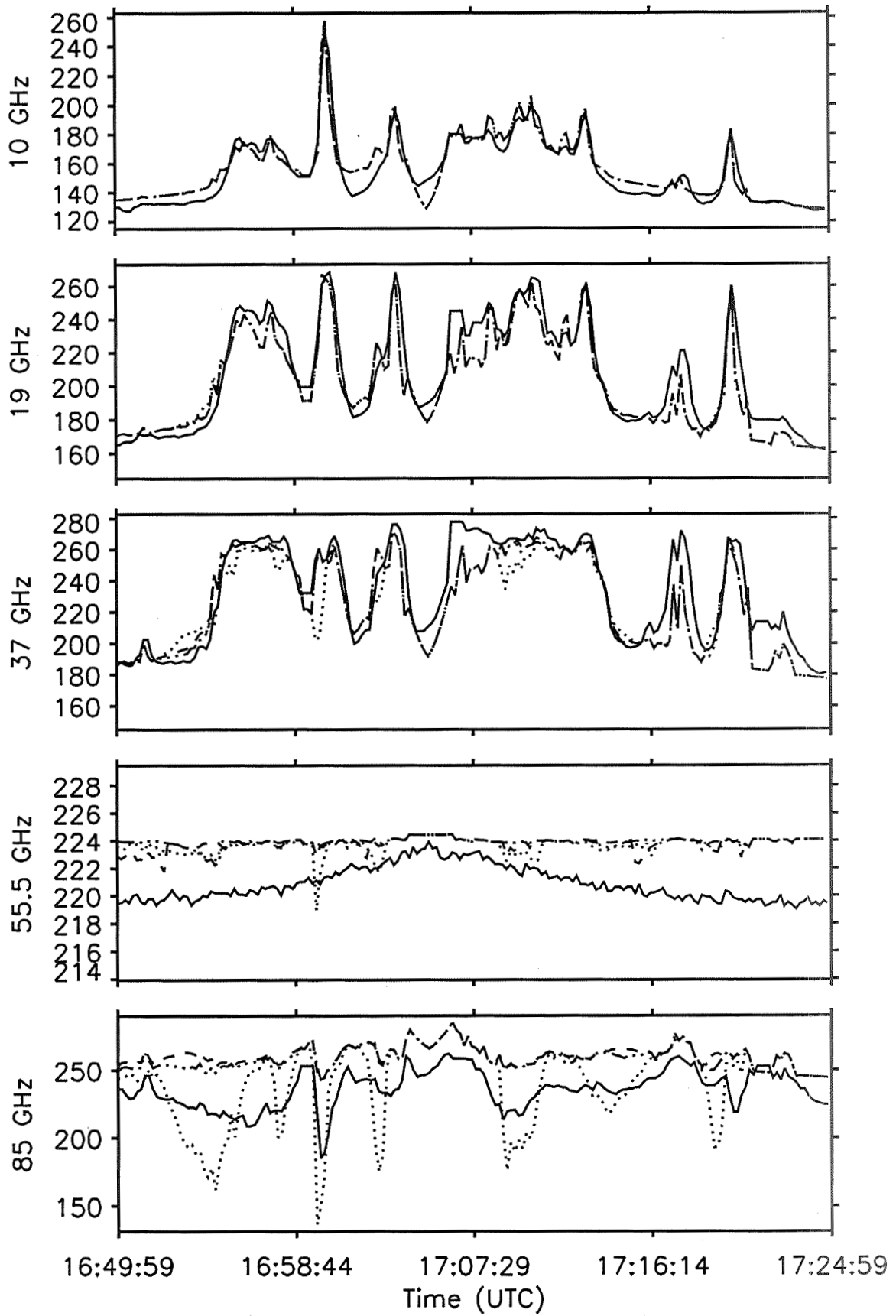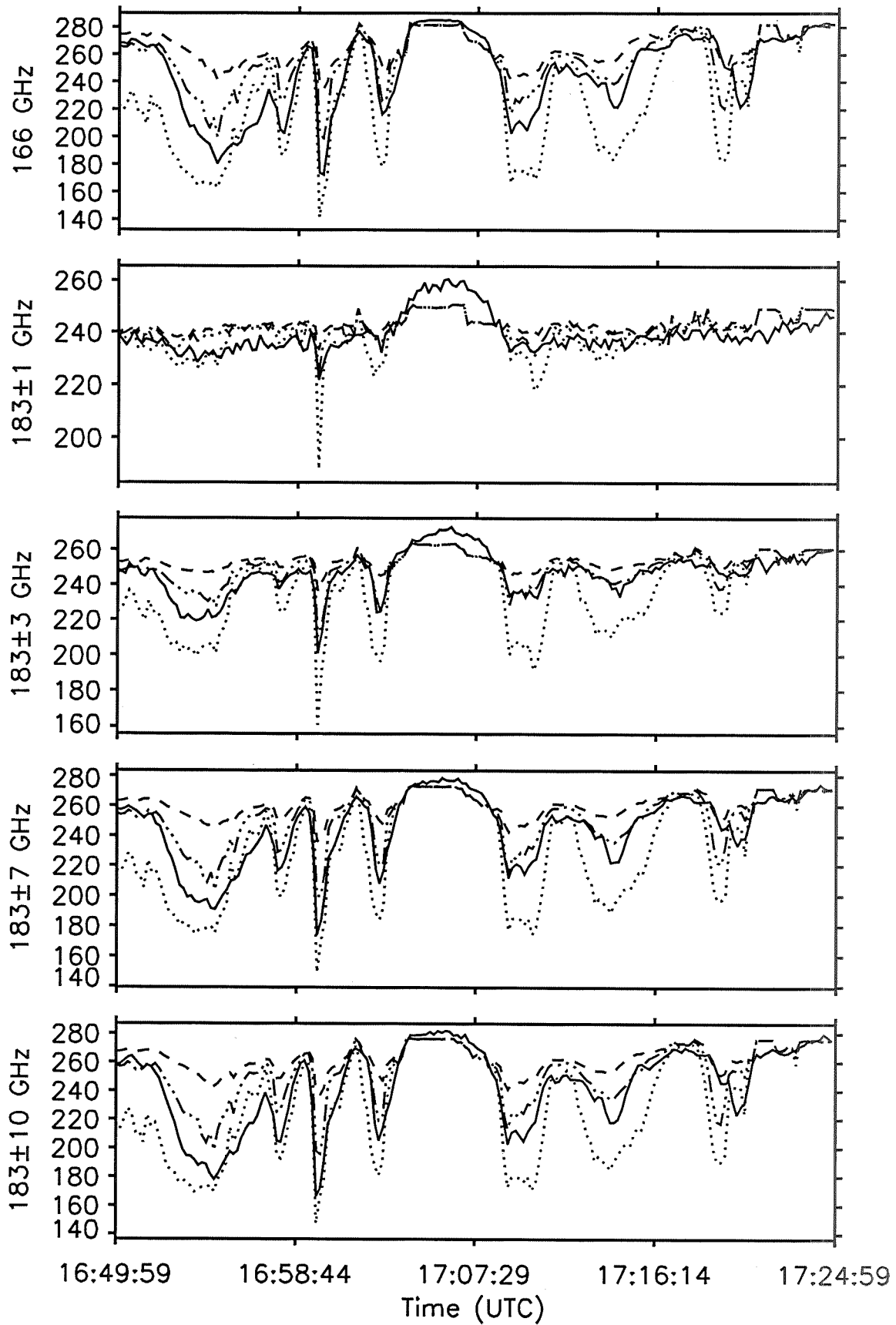
36

Figure 6: Bulk scattering fields at 85 GHz for (a) fluffy spheres, (b) solid ice SS spheres, and (c) three-dimensional rosettes. Shading thresholds are at 0.1, 0.5, 1.0, 2.0, 3.0, and 4.0 nepers/km.
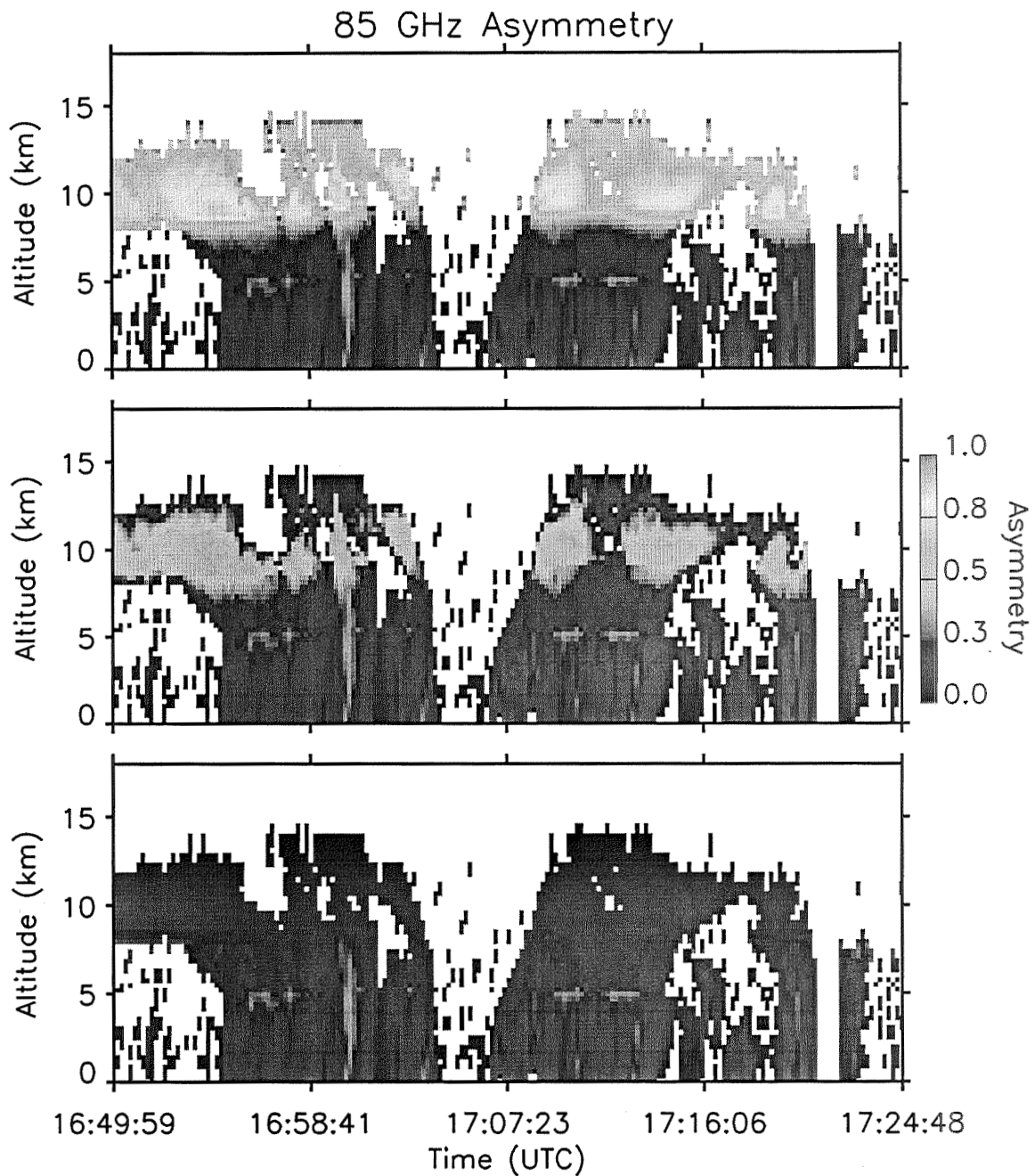
85 GHz Asymmetry

Figure 7: Bulk asymmetry fields at 85 GHz for (a) fluffy spheres, (b) solid ice SS spheres, and (c) three-dimensional rosettes. Asymmetry factors are unitless.

808
809
810
811

38

39

814   Figure 6: Brightness temperature values for 10, 19, 37, 55.5, and 85 GHz in Kelvin for
815   the observations (solid line), SS parameterization (dotted line), Fluffy parameterization
816   (dashed line), and Rosette parameterization (dash-dotted line).
817
818   Figure 7: Same as Figure 6 except for 166, 183.3±1, ±3, ±7, ±10 GHz.